journal of the mechanical behavior of biomedical materials 110 (2020) 103931

Contents lists available at ScienceDirect

Journal of the Mechanical Behavior of Biomedical Materials

journal homepage: http://www.elsevier.com/locate/jmbbm

Estimating tissue-level properties of porcine talar subchondral bone

Lekha Koria, Marlène Mengoni, Claire Brockett *

Institute of Medical and Biological Engineering, School of Mechanical Engineering, University of Leeds, Leeds, LS2 9JT, UK

ARTICLE INFO

Keywords:
Bone biomechanics
Finite element modelling
Ankle
Tissue properties

ABSTRACT

Tissue-level properties of bone play an important role when characterising apparent-level bone biomechanical behaviour and yet little is known about its effect at this hierarchical level. In combination with trabecular morphological data these properties can be used to predict bone strength, which becomes an invaluable tool for clinicians in patient treatment planning.

This study developed specimen-specific micro-finite element (μFE) models using validated continuum-level models, containing grayscale-derived material properties, to indirectly establish tissue-level properties of porcine talar subchondral bone.

Specimen-specific continuum finite element (hFE) models of subchondral trabecular bone were setup using μCT data of ten cylindrical specimens extracted from juvenile porcine tali. The models were validated using quasi-static uniaxial compression testing. Validated hFE models were used to calibrate the tissue modulus of corresponding μFE models by minimising the difference between the μFE and hFE stiffness values. Key trabecular morphological indices (BV/TV, DA, Conn.D, Tb.Th, EF) were evaluated.

Good agreement was observed between hFE models and experiment (CCC = 0.66). Calibrated E_{tiss} was 504 ± 37.65 MPa. Average BV/TV and DA for μFE specimens were 0.37 ± 0.05 and 0.68 ± 0.11, respectively. BV/TV (r^2 = 0.667) correlated highly with μFE stiffness.

The small intra-specimen variation to tissue-level properties suggests that variations to apparent-level stiffness originate from variations to microarchitecture rather than tissue mechanical properties.

1. Introduction

Ankle osteoarthritis is a debilitating, degenerative disease of the talocrural joint. It is predominantly post-traumatic; as many as 80% of cases are thought to be a direct consequence of ankle sprain or trauma (Brown et al., 2006; Valderrabano et al., 2009; Horisberger et al., 2009). Hence, many incidences arise from sports-related injuries (Carbone and Rodeo, 2017; Saltzman et al., 2005; Valderrabano et al., 2009; Arthritis Research UK, 2013), which results in patients requiring treatment earlier than those with osteoarthritis of other joints (Delco et al., 2017). Total ankle arthroplasty offers increased joint mobility, but at the cost of resecting several millimetres of bone from the distal tibia and talar dome (Hintermann and Ruiz, 2014). Low bone stock, typically of poor quality, causes difficulties in achieving stability for device fixation, resulting in stress-shielding, loosening, subsidence and increased fracture risk (Currier et al., 2019; Glazebrook et al., 2009). Consequently, ankle replacement devices have higher revision rates compared to other lower-limb joint replacements (Jackson and Singh, 2003; Egloff et al., 2012). Yet the annual demand for late-stage ankle osteoarthritis treatments is increasing in the UK and the numbers of ankle replacement devices being implanted is rising (Goldberg et al., 2012; NJRS Committee, 2019).

Patient-specific finite element models that evaluate bone quality have the potential to inform surgical planning, evaluate fracture risk and provide clinicians with a better understanding of the biomechanical capabilities of the ankle prior to the implantation of a joint replacement. Macroscopic mechanical properties of bone are predominantly affected by the amount of bone present (bone volume fraction, BV/TV), microarchitecture (anisotropy (DA), trabecular thickness (Tb.Th) etc.) and tissue modulus (E_{tiss}).

A computational approach can be used to circumvent somewhat difficult experiments that require measuring the mechanical properties of individual trabeculae. Using an inverse finite element (FE) approach it is possible to calibrate the stiffness of *in silico* models using macroscopic mechanical tests to indirectly estimate E_{tiss} (van Rietbergen et al., 1995; Bayraktar et al., 2004; Bevill et al., 2009; Mengoni, 2020) and

* Corresponding author.
E-mail address: c.l.brockett@leeds.ac.uk (C. Brockett).

https://doi.org/10.1016/j.jmbbm.2020.103931
Received 26 November 2019; Received in revised form 5 June 2020; Accepted 10 June 2020
Available online 14 July 2020

potentially characterise changes, if any, to tissue-level properties with osteoarthritis. For example, one study analysing early-arthritic specimens in the knee obtained tissue-level properties using specimen-specific inverse FE analysis and showed a decreased bone tissue modulus (Day et al., 2001). To the author's knowledge, tissue-level mechanical properties of subchondral bone in the ankle have not been investigated.

The aim of this study was to develop an inverse FE methodology to estimate tissue modulus from macroscopic mechanical testing of bone cores and image-based, specimen-specific FE models.

2. Materials and methods

A multiscale, computational approach was developed in order to characterise porcine talar subchondral trabecular bone at the tissue level by means of back-calculating tissue properties from validated, continuum models (Fig. 1).

2.1. Experimental specimens

Eight fresh-frozen tali were isolated from juvenile porcine ankles (mean weight = 79.83 kg, Scotlean Ltd and Yorkshire FA, UK). Porcine ankle tissue was chosen for its geometric similarity to human ankles, low cost and high availability from local agri-food industry and hence, does not require ethical review. The frozen tali were fully thawed overnight in a refrigerator at 4 °C before specimen removal. Fifteen cylindrical specimens (6 mm φ) were extracted from the talar dome surface (on average two specimens per tali) using a tubular chisel and hammer. Each tali was kept moist using phosphate-buffered solution (PBS) and extracted specimens were stored in PBS-soaked paper towel to maintain their hydration. The cartilage and subchondral bone plate were removed using a scalpel to leave subchondral cancellous bone specimens of average height 8.63 ± 1.29 mm (6.0–9.9 mm range). The ends of each cylinder were then sanded to a flat-surface and rinsed in PBS. Custom Delrin endcaps were fixed to each end of the specimens using a thin layer of polymethyl-methacrylate cement (PMMA) leaving an average gauge length of 6.23 ± 1.29 mm.

2.2. Imaging

Each specimen was scanned in a μCT (*MicroCT100, ScanCo Medical, Brüttisellen, Switzerland*) at an isotropic resolution of 16 μm (70 kVP, 114 μA, 250 ms integration time) whilst submerged in PBS. The image data was normalised to a 0–255 grayscale (8 bit). Each image stack was cropped to the gauge length height and binarised using Otsu thresholding (*NIH ImageJ 1.52*).

2.3. Mechanical testing

Apparent-level mechanical properties were evaluated using unconfined, quasi-static uniaxial compression testing (*Instron 3365, Instron, High Wycombe, UK*). During testing specimens were immersed in temperature-controlled PBS at 37 °C within a BioBath. Following a preload of 0.3 N for 10 min, each specimen was pre-conditioned at 0.006% s^{-1} for thirty cycles, before being loaded at a quasi-static strain rate of 0.01% s^{-1} to failure. Maximum *in vitro* stiffness, k_{exp}, was derived from the largest slope of the linear-elastic region of the force-(crosshead) displacement raw data. Four specimens were excluded from results as they had displaced laterally during testing. A further specimen was removed from the final dataset due to damage prior to testing. A final total of ten specimens were available for both studies.

2.4. Computational modelling: hFE

Continuum finite element (hFE) models (N = 10) were setup by first downsampling each binarised image stack to a resolution of 0.32 mm whilst taking into account partial volume effects (*Simpleware ScanIP M-2017.06-SP1, Synopsys, California, US*). The bone was segmented using a grayscale threshold and morphological operations. The segmented bone cylinder was meshed with linear tetrahedral elements of approximate 1 mm edge-length following a sensitivity analysis (average number of elements = 2407). The bone was modelled as linear elastic with a Poisson's ratio of 0.3 and a grayscale-dependent elastic modulus. Element-specific elastic modulus (E_{ele}) was defined dependent on the average element grayscale (GS_{ele}) using Equation (1):

$$E_{ele} = \alpha\, GS_{ele}(MPa) \tag{1}$$

To derive the linear proportionality constant, α, specific to this particular type of bone and with these given testing and imaging conditions (Zapata-Cornelio et al., 2017; Day et al., 2020; Wijayathunga et al., 2008), a golden section search scalar optimisation process using the Brent method (Brent, 1971) was used (Mengoni, 2020). Specimens were arbitrarily divided into two groups: calibration (N = 5) and validation (N = 5). Optimisation of the root mean square (RMS) normalised

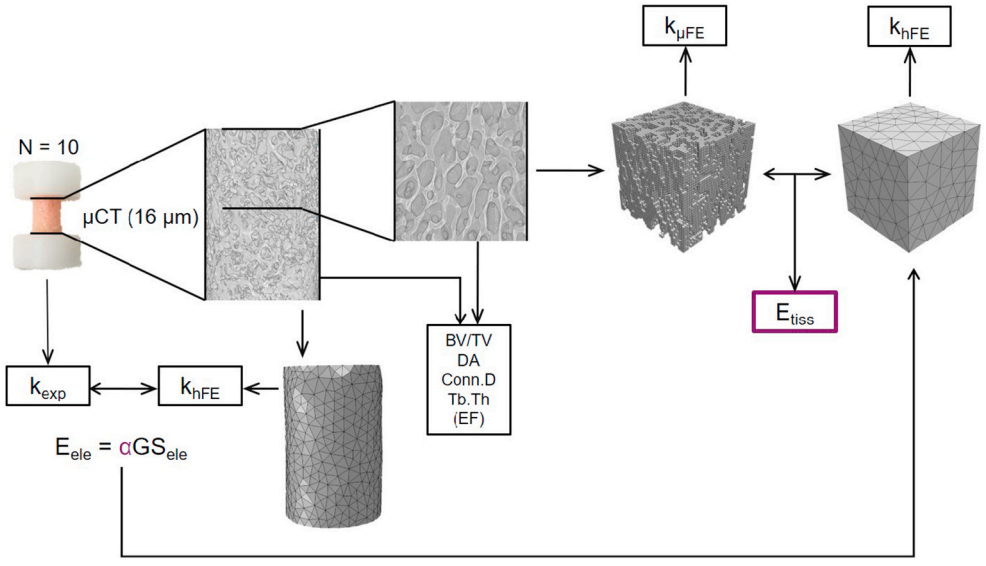

Fig. 1. Methodology to establish tissue-level properties from validated, apparent-level models with calibrated element-specific material properties based on image grayscale.

difference between *in vitro* (k_{exp}) and *in silico* stiffness values was performed on the calibration group using the Opti4Abq toolbox (Mengoni et al., 2015; Mengoni, 2017). Convergence was set at RMSE <10%. The models (N = 5) were validated by scaling the material-properties using α and comparing the output stiffness ($k_{hFE,cyl}$) to k_{exp}. All FE analyses were non-linear quasi-static and performed in parallel with Abaqus (*Simula Abaqus/CAE, 2017; Dassault Systèmes, Velizy-Villacoublay, France*). The experimental unconfined uniaxial compression was simulated *in silico*. All degrees of freedom were constrained on the bottom surface and an axial displacement of −0.3 mm in compression was applied to the top surface with all other degrees of freedom constrained.

2.5. Computational modelling: μFE

Cubic volumes (4 mm length) located at the proximal end of the specimen were extracted from the binarised image stack of each specimen. hFE models (N = 10) were formed using the previously defined protocol with newly validated grayscale-based material properties. Trabecular-level (μFE) analyses (N = 10) were also setup by down-sampling the image stack to a resolution of 0.1 mm. Each voxel was converted to mixed tetrahedral and hexahedral elements (average number of elements = 35965). In both cases, as before, all degrees of freedom were constrained on the bottom surface and an axial displacement of −0.1 mm was applied to the top surface with all other degrees of freedom constrained. Five specimens were used to calibrate tissue elastic modulus through direct comparison of output stiffness to within ± 1% ($k_{hFE,cube}$). This yielded an average tissue modulus, E_{tiss}, which was validated on a further five specimens. An average stiffness, $k_{\mu FE}$, was established from all calibrated models (N = 10) using E_{tiss}. All FE analyses were non-linear quasi-static and performed in Abaqus using local high-performance computing facilities (ARC3, High Performance Computing facilities, University of Leeds).

2.6. Data analysis

The data associated with this paper are openly available from the University of Leeds research data repository (Koria et al., 2020).

Trabecular morphological evaluation was performed using BoneJ (Doube et al., 2010) to evaluate the following properties: BV/TV, DA, Conn.D (connectivity density, mm^{-3}), Tb.Th (mm) and, for the cuboidal specimens used to generate μFE models (Fig. 1), EF (ellipsoid factor) (Doube, 2015; Salmon et al., 2015).

The mean, standard deviation and coefficient of variance (CoV, %) of each morphological, computational and mechanical property was calculated for all specimens. Correlation between: k_{exp} and $k_{hFE,cyl}$; $k_{\mu FE}$ and $k_{hFE,cube}$ and all stiffness values to morphological indices were measured using Square of the Pearson Product-Moment Correlation Coefficient (r^2). Agreement between both k_{exp} and $k_{hFE,cyl}$, and $k\mu_{FE}$ and $k_{hFE,cube}$ were evaluated using Concordance Correlation Coefficient (CCC) values (Lawrence and Lin, 1989) and Bland-Altman analyses. All statistical measures were computed in R (*RStudio 1.1.463*). The Bland-Altman plots were generated with 95% limits of agreement on the verified assumption that the differences to stiffness are normally distributed (Bland and Altman, 1999).

3. Results

3.1. Experimental results

Average stiffness *in vitro*, k_{exp}, was 1140.67 ± 207 N/mm, as derived from the linear elastic portion of the force-displacement plot (Fig. 2).

3.2. Morphological results

For the full cylindrical models, morphological analyses showed that DA (CoV = 18%) and Conn.D (CoV = 24%) had the highest intra-specimen variations. Average values for BV/TV, DA, Tb.Th and Conn.D were: 0.37 ± 0.03, 0.59 ± 0.11, 0.16 ± 0.02 mm and 6.79 ± 1.62 mm^{-3}, respectively.

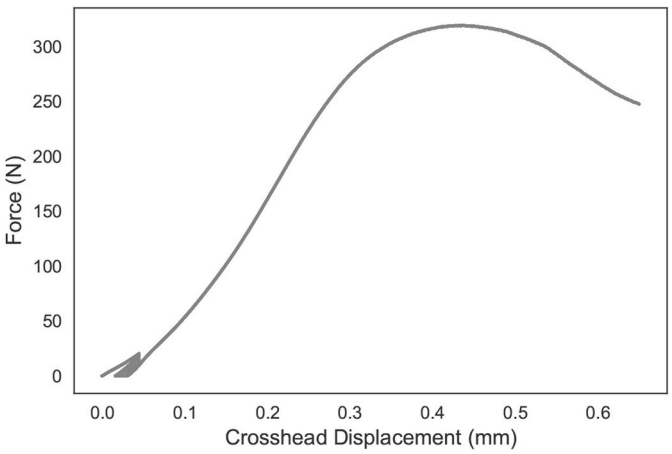

Fig. 2. Exemplary plot of force-displacement for porcine talar subchondral trabecular bone under compression.

For cuboidal specimens, high intra-specimen variations were observed to DA (CoV = 16%) and Conn.D (CoV = 22%). Average values for BV/TV, DA, Tb.Th, Conn.D and EF were 0.37 ± 0.05, 0.68 ± 0.11, 0.16 ± 0.019 mm, 16.81 ± 3.75 mm^{-3} and 0.009 ± 0.05, respectively. EF results indicate that the tissue is a mix of rod-like and plate-like trabeculae.

3.3. Apparent level model calibration and validation

A 69% correlation was found between *in silico* and *in vitro* stiffness values in cylinders (N = 10, Fig. 3a) and showed good agreement (CCC = 0.66, Fig. 3b). The optimisation procedure terminated prior to the set convergence tolerance with a converged value of α rather than a converged RMSE; calibration and validation RMSE were 26% and 17%, respectively. Average apparent-level stiffness was 1066.42 ± 392 N/mm (CoV = 37%) (Fig. 4).

3.4. Trabecular level model calibration and validation

Good correlation ($r^2 = 0.69$) was observed between the hFE and μFE stiffness values in cuboids (Fig. 5a). The optimisation process for each of the calibration samples converged with an RMSE of 7%. Good agreement was observed for validation specimens (N = 5, CCC = 0.75) and optimised specimens (N = 10, CCC = 0.80). Fig. 5b highlights an outlier validation specimen which lies outside of the limits of agreement, which is reflected in the higher RMSE for the validation set (13%) compared to the calibration set (7%). Average E_{tiss} (N = 5) was 504.00 MPa ± 37.65 (CoV = 7%).

3.5. Correlations to microarchitecture

The highest correlations to stiffness was between BV/TV and both k_{exp} ($r^2 = 0.480$) and $k_{\mu FE}$ ($r^2 = 0.667$) (Table 1). Correlations between k_{exp} and Conn.D ($r = -0.34$), and $k_{\mu FE}$ and EF ($r = -0.62$) were both negative.

At the apparent level, both BV/TV and DA account for around 85% of variations to *in silico* stiffness and 60% for *in vitro* stiffness (Fig. 6). At the trabecular level they account for 80% variations to μFE stiffness.

4. Discussion

Specimen-specific models of porcine talar subchondral bone were developed by calibrating the apparent-level relationship between

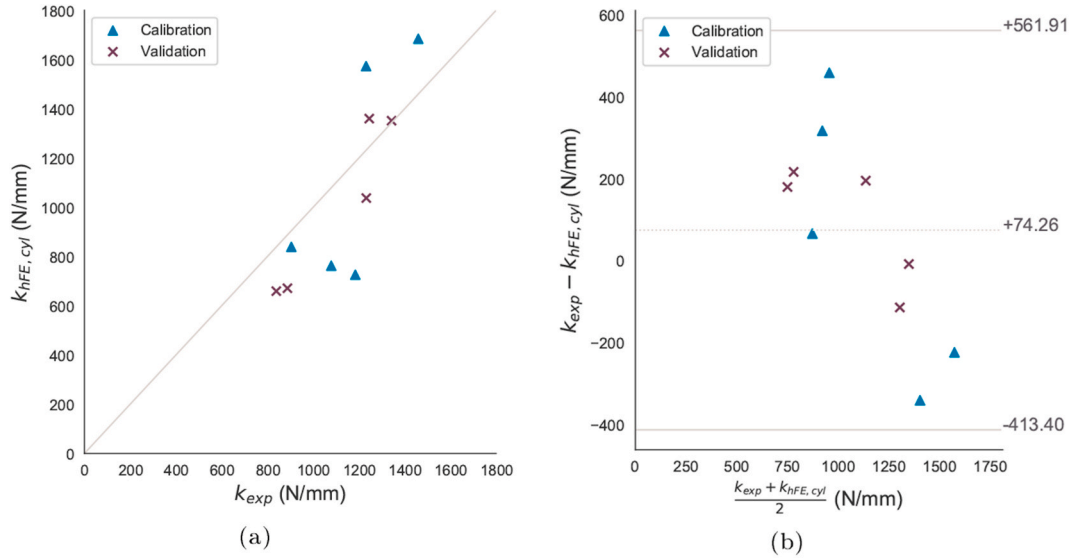

Fig. 3. Results for optimisation of hFE models.
(a) Correlation of experimental stiffness to cylindrical continuum models ($r^2 = 0.69$). (b) Bland-Altman plot showing agreement of experimental stiffness to cylindrical continuum models (CCC = 0.66).

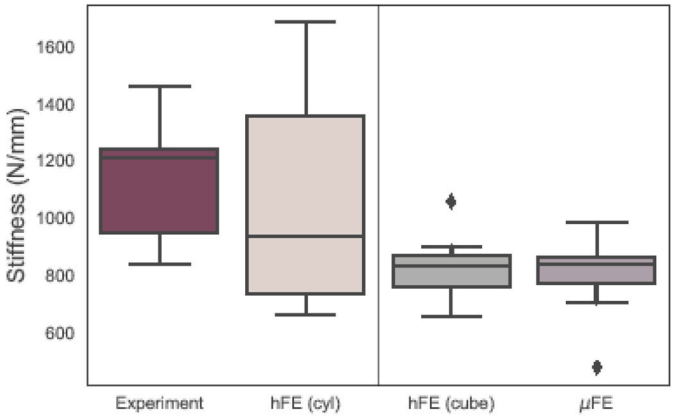

Fig. 4. Experimental and computational stiffness values (N = 10, N/mm) for porcine ankle subchondral bone. A ◆ indicates outlier specimens (specifically, one k_{hFE} calibration specimen and one $k\mu_{FE}$ validation specimen, though not the same specimen).

Young's Modulus and image grayscale with good accuracy. Tissue-level properties were indirectly established by developing and calibrating trabecular-level models using equivalent calibrated continuum models with optimised grayscale-based material properties.

In this study, a low intra-specimen variation of around 7% was observed in tissue modulus. Large variations to tissue modulus can have significant effect on apparent-level mechanical properties, which make comparisons to the effective properties of diseased tissue more difficult, unless variations from microarchitecture are also accounted for. Though a tissue modulus CoV of under 20% is recommended (Jaasma et al., 2002) to avoid large errors in calculated apparent-level properties, some intra-donor variability is inevitable, but can translate to significant differences in effective biomechanical properties. It is therefore key that FE models describe the intra-specimen variability in microarchitecture, as well as variations to material properties in a specimen-specific manner, as demonstrated in this study. Quantifying tissue mechanical properties is essential for accurately predicting the macroscopic biomechanical behaviour of bone. However, calculating tissue properties from simulated apparent-level experiments may result in less-precise measures of tissue modulus (Bevill et al., 2009) compared to results obtained from specimen-specific micro-mechanical testing (Wolfram et al., 2010), and hence this method can only provide an estimate of tissue-level mechanical properties.

Relatively high intra-specimen variations to microarchitecture were observed in this study. Only BV/TV has been reported in other studies for porcine talar bone (den Dunnen et al., 2013), but is higher than reported in this work. Variations of the type of trabeculae present - combinations of rod- and plate-like trabeculae - are known to impact bone strength (Wang et al., 2015). Ellipsoid Factor (EF) is an alternative measure to the structure model index (SMI) in measuring rod-to-plate ratios. It has been argued that SMI does not account for concave surfaces of bone and therefore does not fully represent the geometry of the tissue (Doube, 2015; Salmon et al., 2015). Interestingly, EF was negatively correlated to kμFE; increasing rod-like trabeculae caused a decrease in stiffness. However, it is hard to conclude this is indeed true for all ankle specimens with a limited sample size of ten specimens.

It is well known that the biomechanical behaviour of trabecular bone from multiple anatomical locations can be predominantly described by a combination of BV/TV and DA (Matsuura et al., 2008; Maquer et al., 2015). This was also observed in this study (Fig. 6) where over 65% variations to experimental, hFE and μFE stiffness values originated from BV/TV and DA. This highlights the importance of anisotropy when deriving constitutive relationships between apparent density and elastic modulus. DA had more of an impact on hFE stiffness (45%) than BV/TV (40%). This could be explained by the high variations in anisotropy of the specimens for this model (over 15%), but it is hard to conclude considering the sample size. In this case anisotropy was considered only through inhomogeneous elastic properties, which may explain the sub-optimal correlation and agreement between the experimental and hFE (cyl) simulation stiffness values. However, the errors observed here are similar to that of previous work (Zapata-Cornelio et al., 2017), and the validation error was lower than the calibration error, hence even though sub-optimal agreement was found one can consider the method as valid.

The results in this work demonstrate the methodology to be valid for models to replicate apparent stiffness, however there is no indication of the validity of the strain field it produces. This study also further supports the validity of a linear relationship between image grayscale and apparent stiffness, as employed in other studies (Day et al., 2020; Zapata-Cornelio et al., 2017; Robson Brown et al., 2014; Wijayathunga et al., 2008). Equally, this relationship is limited by its dependency on

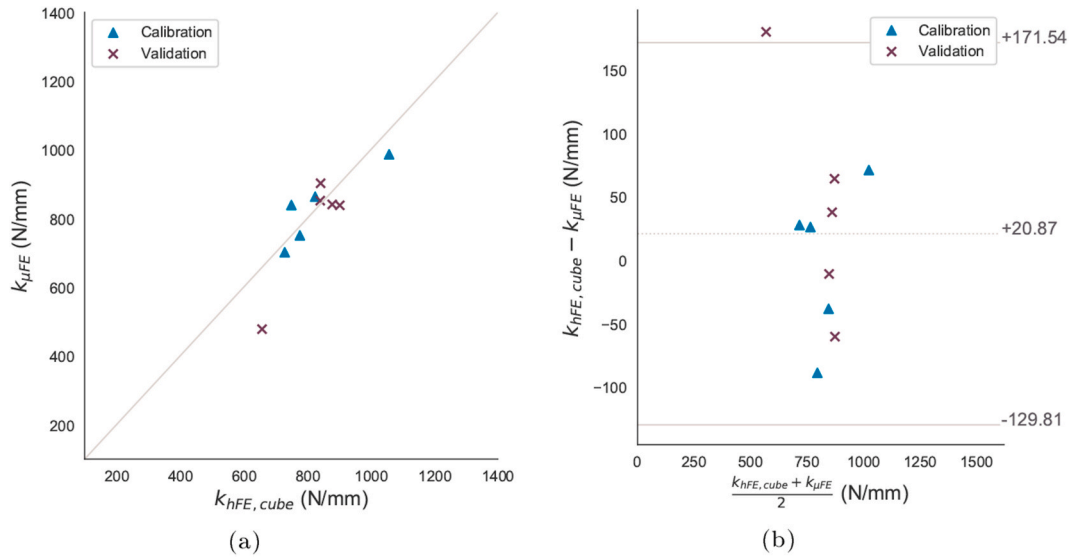

Fig. 5. Results for optimisation of μFE models.
(a) Correlation of continuum-level stiffness to trabecular-level stiffness in cuboids ($r^2 = 0.69$). (b) Bland-Altman plot showing agreement of continuum-level stiffness to trabecular-level stiffness in cuboids (CCC = 0.80).

Table 1
Square of the Pearson Product-Moment Correlation Coefficient (r^2) against microarchitecture and experimental, hFE and μFE stiffness values.

Index	k_{exp} (N/mm)	k_{hFE} (N/mm)	$k_{\mu FE}$ (N/mm)
BV/TV	0.480	0.208	0.667
DA	0.240	0.274	0.228
Conn.D	0.119	0.009	0.005
Tb.Th	0.200	0.005	0.065
EF	–	–	0.380

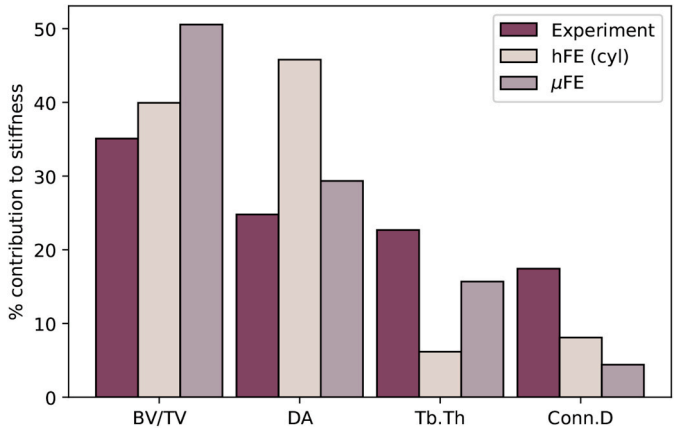

Fig. 6. The percentage correlation of morphological indices on variations in experimental and computational stiffness values as calculated using the correlation coefficient value, *r*. Experimental and hFE stiffness values were compared to morphological evaluation of full cylindrical specimens, whereas μFE stiffness was compared to morphological characterisation of cuboidal specimens.

images acquired using the specific scanner and settings described in this study.

Trabecular-level model optimisation results showed better agreement and higher correlation between stiffness values compared to the apparent level. There was higher variation to apparent-level stiffness for the cylindrical models (37%) compared to the cuboidal models (13%). Selecting a smaller central region may have provided a more accurate representation of the tissue as this eliminates any lateral surface effects. The relatively similar values of microarchitecture measured from the cylinders and the cuboids shows that the cubes are representative of cylinders and hence building μFE models of the full cylinder was unnecessary.

A single specimen in the validation set used for μFE model calibration was found outside the limits of agreement in the Bland-Altman analysis. This specimen had the lowest stiffness values for both hFE and μFE models, as well as a relatively low BV/TV and DA values compared to other specimens. This outlier may therefore affect overall trends to variations in stiffness and microarchitecture. The impact of this specimen is exacerbated by the limited sample size of the study.

Unlike the human talus, the porcine talar dome is more incongruent and features more convex trochlea which created difficulties in accurately extracting uniform, on-axis specimens. Efforts were made to retrieve specimens posteriorly on the talar dome in consideration for the likely loading pattern through the porcine ankle in the hope to retrieve cores that are orientated with the loading direction. It was difficult to extract more than two cores per joint on the talar dome in the posterior region, due to the impact of the hammer and progressive weakening of the bone, causing the talus to fracture. As a result, specimen height varied and most did not satisfy the suggested 2:1 height:diameter ratio for mechanical characterisation (Keaveny et al., 1993), but still satisfied the continuum assumption. Though, this is not an issue as modulus values are not directly derived from experimental data, but are instead derived for exact replication in computational models. Of the fifteen specimens retrieved, four were excluded during testing due to malalignment with the testing platens. These four specimens were also the longest specimens, which may suggest that a higher pre-load was required to secure these specimens in the testing rig. Beyond variation in microarchitecture, variations to *in vitro* stiffness may have originated from varied bone marrow content and surface irregularities in the specimen, which translate to larger variations in density during thresholding. The bone marrow was not removed in this study, but would have negligible effects on mechanical properties at quasi-static strain rates (Carter and Hayes, 1977; Linde et al., 1991). The removal of the marrow may have improved image quality, and in doing so, improve the contrast between bone and its surroundings. This extra step in the specimen preparation phase may also help to remove any residual debris from specimen extraction, which may impact on boundary conditions at the ends of the specimen. Improving thresholding would avoid any appreciable errors in BV/TV and predicting effective mechanical

properties (Bevill et al., 2009).

This study demonstrated that non-diseased porcine talar subchondral trabecular bone has little intra-specimen variation to mechanical properties at the tissue-level, and the estimated tissue modulus was higher than the apparent modulus found *in vitro*. The methods developed in this study can be applied to specimens of non-diseased human ankle bone to estimate tissue mechanical properties, which would then allow for the characterisation of the effective mechanical behaviour of osteoarthritic ankle tissue.

Author statement

Lekha Koria: Conceptualization, Data curation, Formal analysis, Investigation, Methodology, Project administration, Validation, Visualization, Software, Writing – original draft, Writing – review & editing

Marlène Mengoni: Conceptualization, Methodology, Software, Supervision, Writing – review & editing

Claire Brockett: Conceptualization, Funding acquisition, Methodology, Resources, Supervision, Writing – review & editing.

Declaration of competing interest

The authors declare that they have no known competing financial interests or personal relationships that could have appeared to influence the work reported in this paper.

Acknowledgements

This study was funded by the EPSRC (EP/L014823/1). Part of this work was undertaken on ARC3, part of the High Performance Computing facilities at the University of Leeds, UK.

References

Arthritis Research UK, 2013. Osteoarthritis in general practice - data and perspectives - arthritis research UK. The Medical press 222, 253–258.
Bayraktar, H.H., Morgan, E.F., Niebur, G.L., Morris, G.E., Wong, E.K., Keaveny, T.M., 2004. Comparison of the elastic and yield properties of human femoral trabecular and cortical bone tissue. J. Biomech. 37 (1), 27–35.
Bevill, G., Eswaran, S.K., Farahmand, F., Keaveny, T.M., 2009. The influence of boundary conditions and loading mode on high-resolution finite element-computed trabecular tissue properties. Bone 44 (4), 573–578.
Bland, J.M., Altman, D.G., 1999. Measuring agreement in method comparison studies. Stat. Methods Med. Res. 8 (2), 135–160.
Brent, R.P., 1971. An algorithm with guaranteed convergence for finding a zero of a function. Comput. J. 14 (4), 422–425.
Brown, T.D., Johnston, R.C., Saltzman, C.L., Marsh, J.L., Buckwalter, J.A., 2006. Posttraumatic osteoarthritis: a first estimate of incidence, prevalence, and burden of disease. J. Orthop. Trauma 20 (10), 739–744.
Carbone, A., Rodeo, S., 2017. Review of current understanding of post-traumatic osteoarthritis resulting from sports injuries. J. Orthop. Res. 35 (3), 397–405.
Carter, D.R., Hayes, W.C., 1977. The compressive behavior of bone as a two-phase porous structure. JBJS 59 (7), 954–962.
NJRS Committee, 2019. National Joint Registry for England, Wales, Northern ireland and the isle of man: 16th Annual Report. National Joint Registry Centre, 2019.
Currier, B.H., Hecht, P.J., Nunley, J.A., Mayor, M.B., Currier, J.H., Van Citters, D.W., 2019. Analysis of failed ankle arthroplasty components. Foot Ankle Int. 40 (2), 131–138.
Day, J., Ding, M., Van Der Linden, J., Hvid, I., Sumner, D., Weinans, H., 2001. A decreased subchondral trabecular bone tissue elastic modulus is associated with pre-arthritic cartilage damage. J. Orthop. Res. 19 (5), 914–918.
Day, G.A., Jones, A.C., Wilcox, R.K., 2020. Optimizing computational methods of modeling vertebroplasty in experimentally augmented human lumbar vertebrae. JOR Spine, e1077.
Delco, M.L., Kennedy, J.G., Bonassar, L.J., Fortier, L.A., 2017. Post-traumatic osteoarthritis of the ankle: a distinct clinical entity requiring new research approaches. J. Orthop. Res. 35 (3), 440–453.
den Dunnen, S., Mulder, L., Kerkhoffs, G.M., Dankelman, J., Tuijthof, G.J., 2013. Waterjet drilling in porcine bone: the effect of the nozzle diameter and bone architecture on the hole dimensions. J. Mech. Behav.Biomed. Mater. 27, 84–93.
Doube, M., 2015. The ellipsoid factor for quantification of rods, plates, and intermediate forms in 3d geometries. Front. Endocrinol. 6, 15.
Doube, M., Kłosowski, M.M., Arganda-Carreras, I., Cordelières, F.P., Dougherty, R.P., Jackson, J.S., Schmid, B., Hutchinson, J.R., Shefelbine, S.J., 2010. Bonej: free and extensible bone image analysis in imagej. Bone 47 (6), 1076–1079.
Egloff, C., Hügle, T., Valderrabano, V., 2012. Biomechanics and pathomechanisms of osteoarthritis. Swiss Med. Wkly. 142, 0.
Glazebrook, M.A., Arsenault, K., Dunbar, M., 2009. Evidence-based classification of complications in total ankle arthroplasty. Foot Ankle Int. 30 (10), 945–949.
Goldberg, A.J., MacGregor, A., Dawson, J., Singh, D., Cullen, N., Sharp, R.J., Cooke, P.H., 2012. The demand incidence of symptomatic ankle osteoarthritis presenting to foot & ankle surgeons in the United Kingdom. Foot 22 (3), 163–166.
Hintermann, B., Ruiz, R., 2014. Ankle arthritis and the treatment with ankle replacement. Revista Médica Clínica Las Condes 25 (5), 812–823.
Horisberger, M., Valderrabano, V., Hintermann, B., 2009. Posttraumatic ankle osteoarthritis after ankle-related fractures. J. Orthop. Trauma 23 (1), 60–67.
Jaasma, M.J., Bayraktar, H.H., Niebur, G.L., Keaveny, T.M., 2002. Biomechanical effects of intraspecimen variations in tissue modulus for trabecular bone. J. Biomech. 35 (2), 237–246.
Jackson, M., Singh, D., 2003. Total ankle replacement. Curr. Orthop. 17 (4), 292–298.
Keaveny, T.M., Borchers, R.E., Gibson, L.J., Hayes, W.C., 1993. Trabecular bone modulus and strength can depend on specimen geometry. J. Biomech. 26 (8), 991–1000.
Koria, L., Mengoni, M., Brockett, C., 2020. Estimating Tissue-level Properties of Porcine Talar Subchondral Bone - dataset. University of Leeds [Dataset]. https://doi.org/10.5518/787.
Lawrence, I., Lin, K., 1989. A concordance correlation coefficient to evaluate reproducibility. Biometrics 255–268.
Linde, F., Nørgaard, P., Hvid, I., Odgaard, A., Søballe, K., 1991. Mechanical properties of trabecular bone. dependency on strain rate. J. Biomech. 24 (9), 803–809.
Maquer, G., Musy, S.N., Wandel, J., Gross, T., Zysset, P.K., 2015. Bone volume fraction and fabric anisotropy are better determinants of trabecular bone stiffness than other morphological variables. J. Bone Miner. Res. 30 (6), 1000–1008.
Matsuura, M., Eckstein, F., Lochmüller, E.-M., Zysset, P.K., 2008. The role of fabric in the quasi-static compressive mechanical properties of human trabecular bone from various anatomical locations. Biomech. Model. Mechanobiol. 7 (1), 27–42.
Mengoni, M., 2017. opti4abq, a generic python code to run abaqus in an optimisation loop. https://doi.org/10.5281/zenodo.557057 [Software].
Mengoni, M., 2020. Using inverse finite element analysis to identify spinal tissue behaviour in situ. Methods. https://doi.org/10.1016/j.ymeth.2020.02.004.
Mengoni, M., Luxmoore, B., Jones, A., Wijayathunga, V., Broom, N., Wilcox, R., 2015. Derivation of inter-lamellar behaviour of the intervertebral disc annulus. J. Mech. Behav. Biomed. Mater. 48, 164–172.
Robson Brown, K., Tarsuslugil, S., Wijayathunga, V., Wilcox, R., 2014. Comparative finite-element analysis: a single computational modelling method can estimate the mechanical properties of porcine and human vertebrae. J. R. Soc. Interface 11 (95), 20140186.
Salmon, P.L., Ohlsson, C., Shefelbine, S.J., Doube, M., 2015. Structure model index does not measure rods and plates in trabecular bone. Front. Endocrinol. 6, 162.
Saltzman, C.L., Salamon, M.L., Blanchard, G.M., Huff, T., Hayes, A., Buckwalter, J.A., Amendola, A., 2005. Epidemiology of ankle arthritis: report of a consecutive series of 639 patients from a tertiary orthopaedic center. Iowa Orthop. J. 25, 44.
Valderrabano, V., Horisberger, M., Russell, I., Dougall, H., Hintermann, B., 2009. Etiology of ankle osteoarthritis. Clin. Orthop. Relat. Res. 467 (7), 1800–1806.
van Rietbergen, B., Weinans, H., Huiskes, R., Odgaard, A., 1995. A new method to determine trabecular bone elastic properties and loading using micromechanical finite-element models. J. Biomech. 28 (1), 69–81.
Wang, J., Zhou, B., Liu, X.S., Fields, A.J., Sanyal, A., Shi, X., Adams, M., Keaveny, T.M., Guo, X.E., 2015. Trabecular plates and rods determine elastic modulus and yield strength of human trabecular bone. Bone 72, 71–80.
Wijayathunga, V., Jones, A., Oakland, R., Furtado, N., Hall, R., Wilcox, R., 2008. Development of specimen-specific finite element models of human vertebrae for the analysis of vertebroplasty. Proc. IME H J. Eng. Med. 222 (2), 221–228.
Wolfram, U., Wilke, H.-J., Zysset, P.K., 2010. Valid μ finite element models of vertebral trabecular bone can be obtained using tissue properties measured with nanoindentation under wet conditions. J. Biomech. 43 (9), 1731–1737.
Zapata-Cornelio, F.Y., Day, G.A., Coe, R.H., Sikora, S.N., Wijayathunga, V.N., Tarsuslugil, S.M., Mengoni, M., Wilcox, R.K., 2017. Methodology to produce specimen-specific models of vertebrae: application to different species. Ann. Biomed. Eng. 45 (10), 1–10.